

A novel method for improving damage detectability in nonlinear wave modulation: Modeling and design of a driving system

Naserodin Sepehry

Shahrood University of Technology

Sina Asadi

Amirkabir University of Technology

Mohammad Ehsani

Amirkabir University of Technology

Weidong Zhu

UMBC: University of Maryland Baltimore County

Firooz Bakhtiari Nejad (✉ bakhtiari@aut.ac.ir)

University of Maryland Baltimore County <https://orcid.org/0000-0002-7639-1242>

Research Article

Keywords: Nonlinear Wave Modulation, Circuit, Inductor, Aluminum beam, Sandwich Panel, Low Cost System, Structural Health Monitoring, Bolt loosening, Boundary loosening

Posted Date: June 23rd, 2022

DOI: <https://doi.org/10.21203/rs.3.rs-1727959/v1>

License:  This work is licensed under a Creative Commons Attribution 4.0 International License.

[Read Full License](#)

A novel method for improving damage detectability in nonlinear wave modulation: Modeling and design of a driving system

Naserodin Sepehry · Sina Asadi · Mohammad Ehsani · Weidong Zhu · Firooz Bakhtiari Nejad

the date of receipt and acceptance should be inserted later

Abstract Nonlinear wave modulation (NWM) is a nonlinear health monitoring technique that allows for the early detection of minor faults and damages. The purpose of this study is to develop a novel, low-cost and portable device to improve the damage index (DI) in the NWM. 2D spectral finite element method is used to model the electromechanical coupling between piezoelectric patches, an inductor and a structure in a feasibility study. In the simulation, an inductor is attached to each actuator to compare the results with those without an inductor. A specific inductance value is selected for the piezoelectric transducer to achieve resonance, which results in an increased voltage amplitude. A circuit that is inexpensive and portable has been designed and implemented. The results of two experimental setups, an aluminum beam with boundary loosening and a sandwich panel with bolt loosening as damage, are compared with those of the NWM without an inductor. The average of sidebands as a DI is then compared for various frequency combinations using the two NWM techniques i.e. with and without an inductor.

Keywords Nonlinear Wave Modulation · Circuit · Inductor · Aluminum beam · Sandwich Panel · Low Cost System · Structural Health Monitoring · Bolt loosening · Boundary loosening

1 Introduction

One of the most researched areas in structural health monitoring (SHM) in the last two decades has been the early detection of damage using nonlinear characteristics of elastic waves [1–5]. Some previous studies have used linear methods in SHM [6–8]. The piezoelectric patches can be used for

Naserodin Sepehry

Faculty of Mechanical and Mechatronic Engineering, Shahrood University of Technology, Shahrood

Sina Asadi

New Technologies Research Center (NTRC), Amirkabir University of Technology, Tehran

Mohammad Ehsani

New Technologies Research Center (NTRC), Amirkabir University of Technology, Tehran

Weidong Zhu

Department of Mechanical Engineering, University of Maryland, Baltimore County, USA

Firooz Bakhtiari Nejad (Corresponding Author)

Department of Mechanical Engineering, Amirkabir University of Technology, Tehran E-mail: baktiari@aut.ac.ir

Department of Engineering, University of Loyola, Maryland, USA E-mail: fbnejad@loyola.edu

online monitoring of structures [6,9–12]. As opposed to linear damage detection methods, nonlinear methods detect damage at an earlier stage [13]. There is evidence that nonlinear methods, such as the subharmonic resonance method [14], the second-order output [15,16], and the higher-order harmonic method [17], can be used to detect defects in structures.

Various experimental methods detect non-classical damage [18–20]. So far, the technique of nonlinear methods have been used to detect damage in a wide range of structures, including reinforced sheets, welded pipe fittings [21], bolts looseness [22–31], structure with fatigue cracks [32–36], and composite structures [37–39]. Nonlinear wave modulation (NWM) is one of the nonlinear methods for detecting damage. The main concept of NWM is to apply a pump and carrier wave to the structure. The structure is subjected to both of these waves at the same time. If the structure is perfectly linear, the response spectrum will only contain the main frequency components, namely, the probe (carrier) and pump frequencies. A nonlinear structure is characterized by higher harmonics and sidebands around the carrier frequency in addition to the linear components of the response spectrum [10,40]. Nonlinear damage indices (DIs) are negligible due to the low severity of damage in the early stages. As a result, the probability of successfully detecting damage in a noisy environment is reduced.

Depending on the frequency range used to stimulate the pump, there are two types of inter-modulation techniques. They are similar in terms of the principle of detecting damage, but differ slightly in terms of implementation, simulation, and signal processing. In the first type, called vibro-acoustic modulation (VAM), the pump signal corresponds to one of the structure's first natural frequencies (less than 1500 Hz in most previous studies). In this paper, a second type of signal was used, NWM, which uses an ultrasonic pump signal [41–43]. Although the results of VAM and NWM can be studied in both the time and frequency domains, frequency domain results are frequently employed to offer effective damage indicators in practice. The modulation phenomenon occurs as a sideband around the carrier frequency peak at frequencies $f_c \pm n f_p$ ($n = 1, 2, \dots$), where f_c is the carrier frequency, f_p is the pump frequency and n is the sideband number. Sohn et al. proposed the NWM for detecting sidebands that employ a high frequency and low voltage (10 V) pump actuation [40].

In practical implementation, pump excitation in VAM is often applied with shakers [29,34,44,45] or piezoelectric stacks [27]. Shakers can inject considerable of energy into the structure; however, they are challenging to be implemented in online monitoring applications. In addition, nonlinear contact behavior at the point of contact of the shaker with the structure is likely. Due to their high operation bandwidth, piezoelectric patches, can be used for VAM and NWM. In most papers that use NWM, a function generator is used to apply voltage to the carrier and pump actuators. An oscilloscope or digitizer was used to measure the sensor voltage. Liu et al. [46] developed a wireless sensor node for fatigue crack detection. In order to calculate the damage indicator, Oppermann et al. [47] used undersampling and a sensor network, which reduced computational resources and memory requirements significantly. Only one pair of sidebands has been observed at the sensor frequency response output in most earlier works that employed 10 V for actuators. The key to defect identification in the NWM method is to maximize nonlinear effects by optimal excitation of surfaces in contact by combined stimulations [29,48]. However, heavy and expensive amplifiers are required for higher voltages [28,34,39,41].

The previous studies demonstrated that increasing the voltage causes the DI to increase. In online detection methods, the heavy and bulky amplifiers can be difficult to use, but if they are not used, they reduce the signal-to-noise ratio in environments with high levels of noise, resulting in a reduction in the amplitude of sidebands, or failing to detect them in defective structures. This paper describes the design and implementation of a portable and low-cost device for improving NWM. A piezoelectric transducer and an inductor are used to form a circuit between the wave generator and the actuator, thus increasing the efficiency of the NWM. A feasibility analysis is

first conducted with an electromechanical coupled model of piezoelectric, inductor, and beam with the loosened boundary as damage. A device has been developed and tested on an aluminum beam with a loosened boundary and a sandwich panel with a loosened bolt.

2 Model description

This section introduces an electromechanical coupled model developed via 2D spectral finite element (SFEM) to investigate the proposed concept of increasing the performance of the NWM. The beam with dimensions of $300 \times 20 \times 1 \text{ mm}^3$ is modeled (Figure (1)), with the loose boundary as the defect. The beam has three piezoelectric transducers mounted on it. These PZTs functions as a

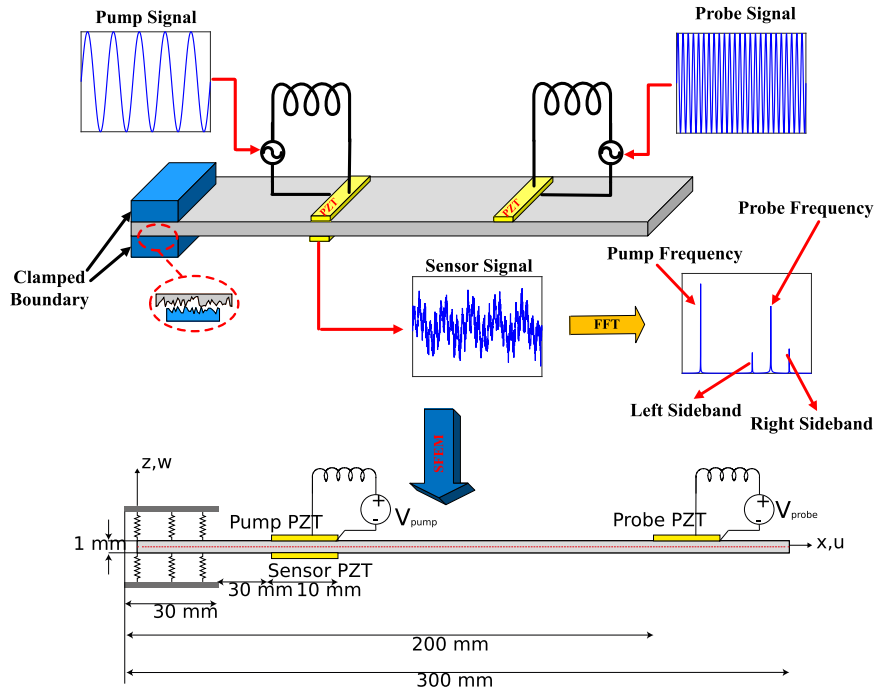


Fig. 1: Schematic of the beam with piezoelectric transducers and inductors.

pump, probe and sensor (Figure (1)). An inductor is attached to each actuator PZT to increase the input voltage of the NWM (Figure (1)). The inductor is seriated with the actuator PZT to create a resonance circuit, which increases the applied voltage at a specific frequency. For the actuator PZT and the inductor to resonate at a specified frequency, it is necessary to change the inductor value. The boundary conditions for the beam consist of a region of the beam which is in contact with the support. Mating surfaces with higher stiffness are designated as "secondary", while those with lower stiffness are designated as "primary". As a result, the primary is the support, whereas the secondary is the beam surface in contact with the support (Figure (1)). The node-to-node formulation is utilized to maintain the contact between mating surfaces. The Lagrange multiplier formulation is used to enforce the constrained conditions. The sinusoidal voltage input is applied

directly to the top of the actuator PZT in the first case while for the second simulation, the voltage is applied to the PZT through the inductor.

2.1 2D spectral element method

The geometry of the 6×6 2D spectral element is shown in Figure (2). 2D displacements can be

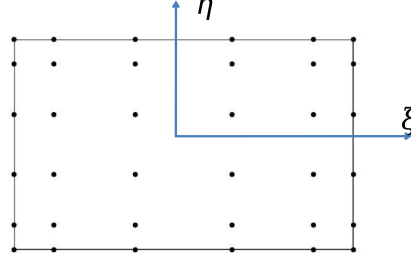


Fig. 2: Geometry of spectral element.

defined as follow:

$$\begin{aligned}
 u(\xi, \eta) &= \sum_i \sum_j N_i(\xi) N_j(\eta) u_{ij} \\
 w(\xi, \eta) &= \sum_i \sum_j N_i(\xi) N_j(\eta) w_{ij}
 \end{aligned} \tag{1}$$

where u_{ij} and w_{ij} are nodal displacements. i and j denote the index of nodes in the ξ and η direction, respectively. N_i and N_j are the shape functions.

In each element, the \mathbf{N} matrix, which relates displacement fields to nodal displacements, can be expressed as:

$$\begin{aligned}
 \mathbf{u} &= \mathbf{N} \mathbf{d} \\
 \mathbf{d} &= \{ \mathbf{d}_{11} \ \mathbf{d}_{12} \ \cdots \ \mathbf{d}_{n_1 n_2} \} \\
 \mathbf{d}_{ij} &= \{ u_{ij} \ w_{ij} \} \\
 \mathbf{N} &= [\mathbf{N}_{11} \ \mathbf{N}_{12} \ \cdots \ \mathbf{N}_{n_1 n_2}] \\
 \mathbf{N}_{ij} &= \begin{bmatrix} N_i(\xi) N_j(\eta) & 0 \\ 0 & N_i(\xi) N_j(\eta) \end{bmatrix}
 \end{aligned} \tag{2}$$

In both structural and PZT elements, the \mathbf{B}_u matrix, which relates nodal displacements to strain field, is represented by

$$\begin{aligned}
 \boldsymbol{\varepsilon} &= \mathbf{B}_u \mathbf{d} \\
 \boldsymbol{\varepsilon} &= [\varepsilon_{xx} \ \varepsilon_{zz} \ \varepsilon_{xz}] \\
 \mathbf{B}_u &= [\mathbf{B}_{11} \ \mathbf{B}_{12} \ \cdots \ \mathbf{B}_{n_1 n_2}] \\
 \mathbf{B}_{ij} &= \begin{bmatrix} \frac{\partial}{\partial x} & 0 \\ 0 & \frac{\partial}{\partial y} \\ \frac{\partial}{\partial y} & \frac{\partial}{\partial x} \end{bmatrix} N_i(\xi) N_j(\eta)
 \end{aligned} \tag{3}$$

It is assumed that the electric potential of the PZT layer is distributed linearly through the thickness [49]. So, the electric voltage ϕ_p in the PZT can be calculated by

$$E_z = -\frac{\partial\phi_p}{\partial z} = -\frac{\phi}{h_p} = -\mathbf{B}_\varphi\varphi \quad (4)$$

The beam and PZT mass matrix elements can be defined as:

$$\begin{aligned} \mathbf{M}^e &= \int \int \int_V \rho \mathbf{N}^T \mathbf{N} |\mathbf{J}| dV \\ \mathbf{K}^e &= \int \int \int_V \left(\mathbf{B}_u^T \mathbf{D} \mathbf{B}_u + \mathbf{N}^T \mathbf{K}_s \mathbf{N} \right) |\mathbf{J}| dV \end{aligned} \quad (5)$$

where

$$\mathbf{K}_s = \begin{bmatrix} 0 & 0 \\ 0 & k_s \end{bmatrix} \quad (6)$$

where \mathbf{J} is the Jacobian matrix of the element, ρ and \mathbf{D} are density and elastic matrix, respectively. V is the volume of element. k_s is the spring constant of elastic foundation. For elements lacking a spring $k_s = 0$. The superscript T represent the transpose operation.

According to piezoelectric constitutive equations, for PZT element, we have [11]:

$$\begin{aligned} \mathbf{K}_{u\varphi}^i &= \mathbf{K}_{\varphi u}^i{}^T = \int \int \int_{V^i} \mathbf{B}_u^T \mathbf{e}^T \mathbf{B}_\varphi |\mathbf{J}| dV \\ \mathbf{K}_{\varphi\varphi}^i &= \int \int \int_{V^i} \mathbf{B}_\varphi^T \boldsymbol{\varepsilon}^S \mathbf{B}_\varphi |\mathbf{J}| dV \end{aligned} \quad (7)$$

where V^i is the element volume of PZT and superscript i is pump, probe and sensor. \mathbf{e} is the piezoelectric coupling coefficients for stress-charge form and $\boldsymbol{\varepsilon}^S$ is electric permittivity.

The differential equation of the global system with adding Rayleigh's damping ($\mathbf{C} = \alpha \mathbf{M} + \beta \mathbf{K}$) is given by [49]:

$$\begin{aligned} \mathbf{M}\ddot{\mathbf{d}} + \mathbf{C}\dot{\mathbf{d}} + \mathbf{K}\mathbf{d} &= -\mathbf{K}_{u\varphi}^{pu} \varphi^{pu} - \mathbf{K}_{u\varphi}^{pr} \varphi^{pr} \\ \mathbf{K}_{\varphi\varphi}^s \varphi^s &= -\mathbf{K}_{\varphi u}^s \mathbf{d} \end{aligned} \quad (8)$$

where φ^{pu} and φ^{pr} are the applied voltage to the pump and probe actuator, respectively. φ^s is output voltage of the sensor. α and β are Rayleigh coefficients.

2.2 Coupling SFEM with the circuit

A study of the electromechanical equations of the PZT with the circuit is presented in this section. Eq. (4) and piezoelectric constitutive equations can be used to calculate the output charge of the PZT pump and probe actuator.

$$Q^i(t) = \int \int_{A^i} D dA = \int \int_{A^i} \left(\mathbf{e} \mathbf{B}_u \mathbf{d} + \frac{\varepsilon_{33}^S \varphi^i}{h_p^i} \right) dA = \int \int_{A^i} (\mathbf{e} \mathbf{B}_u) dA \mathbf{d} + C^i \varphi^i \quad (9)$$

where:

$$C^i = \frac{\varepsilon_{33}^S A^i}{h_p^i} \quad (10)$$

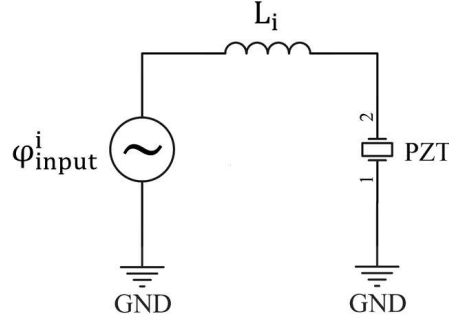


Fig. 3: circuit of PZT with inductor

where A^i is the area of pump and probe elements. where superscript i is the pump and probe actuator. The differential equations governing the electrical circuit that contains the PZT actuator and the inductor are as follow (Figure (3)):

$$L^i \frac{d^2 Q^i(t)}{dt^2} + \varphi^i = \varphi_{inp}^i \quad (11)$$

where φ_{inp}^i is the input voltage. L^i is the inductance of inductor connected to the pump and probe PZTs. As the inductor has a small inherent resistance, this resistance has been omitted from the calculations.

The final coupled equation can be rewritten as follow:

$$\begin{cases} \mathbf{M}\ddot{\mathbf{d}} + \mathbf{C}\dot{\mathbf{d}} + \mathbf{K}\mathbf{d} = -\mathbf{K}_{\mathbf{u}\varphi}^{pu} \varphi^{pu} - \mathbf{K}_{\mathbf{u}\varphi}^{pr} \varphi^{pr} \\ Q^{pu}(t) = \iint_{A^{pu}} (\mathbf{e}\mathbf{B}_{\mathbf{u}}) dA d + C^{pu} \varphi^{pu} \\ Q^{pr}(t) = \iint_{A^{pr}} (\mathbf{e}\mathbf{B}_{\mathbf{u}}) dA d + C^{pr} \varphi^{pr} \\ L^{pu} \frac{d^2 Q^{pu}(t)}{dt^2} + \varphi^{pu} = \varphi_{inp}^{pu} \\ L^{pr} \frac{d^2 Q^{pr}(t)}{dt^2} + \varphi^{pr} = \varphi_{inp}^{pr} \\ \mathbf{K}_{\varphi\varphi}^s \varphi^s = -\mathbf{K}_{\varphi\mathbf{u}}^s \mathbf{d} \end{cases} \quad (12)$$

Solving these equations yields the output voltage of the sensor.

2.3 Investigation of the effect of an inductor on actuator voltage in the linear case

The inductor effect on the voltage of the PZT actuator is investigated in this section. In this case, only the voltage on the pump actuator is checked (the applied voltage of the probe is taken to be zero). However, the results can be extended to the probe actuator as well. A sinusoidal voltage is assumed to be applied to the circuit with the inductor and PZT ($\varphi_{inp}^{pu} = \Phi \cos(\omega t)$ and $\varphi_{inp}^{pr} = 0$, where Φ is the amplitude of input voltage). Based on Eq. (12) and the linear assumption, the solution of the equations in linear mode is as follows:

$$\begin{cases} \varphi^{pu}(t) = \Phi_0^{pu} e^{i\omega t} \\ \mathbf{d} = \mathbf{d}_0 e^{i\omega t} \end{cases} \quad (13)$$

So, we have:

$$\left\{ \begin{array}{l} \mathbf{d}_0 = -(-M\omega^2 + Ci\omega + \mathbf{K})^{-1} \mathbf{K}_{\mathbf{uV}}^{pu} \Phi_0^{pu} \\ Q_0^{pu}(t) = \left(\underbrace{\iint_{A^{pu}} (\mathbf{eB}_u) dA}_{Q_0^{pu}} + C^{pu} \Phi_0^{pu} \right) e^{i\omega t} \end{array} \right. \quad (14)$$

Substitute Eq. (14) to Eq. (11), we have

$$(-L^{pu}\omega^2) Q_0^{pu} + \Phi_0^{pu} = \Phi \quad (15)$$

According to the Eqs. (13), (14) and (15), the voltage applied to the PZT actuator is equal to:

$$\Phi_0^{pu} = \left(L^{pu}\omega^2 \int \int_{A^{pu}} \mathbf{eB}_u dA (-M\omega^2 + Ci\omega + \mathbf{K})^{-1} \mathbf{K}_{\mathbf{uV}}^{pu} + (-L^{pu}\omega^2 C^{pu} + 1) \right)^{-1} \Phi \quad (16)$$

According to Eq. (15) and in the absence of an inductor ($L^{pu} = 0$), the voltage applied to the PZT actuator is equal to Φ . In Eq. (16), the value of ω is selected as follows:

$$\omega = \sqrt{\frac{1}{C^{pu} L^{pu}}} \quad (17)$$

So, the voltage of is applied to the PZT actuator as follows:

$$\Phi_0^{pu} = \left(\frac{1}{C^{pu}} \int \int_{A^{pu}} \mathbf{eB}_u dA \left(-M \frac{1}{L^{pu} C^{pu}} + Ci \sqrt{\frac{1}{L^{pu} C^{pu}}} + \mathbf{K} \right)^{-1} \mathbf{K}_{\mathbf{uV}}^{pu} \right)^{-1} \Phi \quad (18)$$

In NWM, both the pump and probe frequencies are commonly selected above 10 kHz [40]. High structural damping in these frequency regions, reduce the effects of structural resonance relative to low frequencies [11]. According to Eqs. (16) and (18), by selecting an appropriate inductor at the intended frequency, the energy supplied by the input voltage is transferred from the capacitive part of the PZT to the coupling part. Hence, the applied voltage to the actuator PZTs (pump and probe) is increased which is appealing for NWM fault diagnosis. Finally, Eq. (17) can be used to calculate the inductor value based on the desired frequency.

2.4 Nonlinear Equation of contact between beam and support

Contact problems are generally nonlinear phenomena. In this section, Lagrange multipliers are used to solve the equations of motion with contact conditions. The first step is to formulate the restrained equation of motion. The next step involves introducing the Lagrange multiplier. After this, the equations of motion are solved by following a time stepping procedure. Since the slip is tiny, only normal contact is introduced [50].

2.4.1 The gap function definition

The displacement constraints have been imposed to prevent the primary nodes from penetrating the secondary domain. These constraints are as follows [49]:

$$\mathbf{g}_N = \mathbf{G}_N(\mathbf{d} + \delta \mathbf{e}_S) \quad (19)$$

The displacement at nodes is \mathbf{d} and the spring free length is $\delta = 10^{-10}$. Additionally, $\mathbf{e}_S = \sum_{i \in S} \mathbf{e}_i$, where S represents a set of activated nodal contacts and \mathbf{e}_i represents a unit vector in normal direction.

Displacement and deformation change \mathbf{G}_N 's components *a priori*. To introduce restrained displacement components into \mathbf{G}_N when the contact occurs, the motions of the contactor and target must be tracked.

2.4.2 Lagrange multiplier method

By inserting the Lagrange multipliers into Eq. (12), we get:

$$\begin{cases} \mathbf{M}\ddot{\mathbf{d}} + \mathbf{C}\dot{\mathbf{d}} + \mathbf{K}\mathbf{d} + \mathbf{G}_N^T \boldsymbol{\lambda}_N = -\mathbf{K}_{\mathbf{u}\varphi}^{pu} \varphi^{pu} - \mathbf{K}_{\mathbf{u}\varphi}^{pr} \varphi^{pr} \\ \mathbf{G}_N(\mathbf{d} + \delta \mathbf{e}_S) \geq 0; \quad \boldsymbol{\lambda}_N \leq \mathbf{0}; \quad \mathbf{g}_N^i \boldsymbol{\lambda}_N^i = 0 \text{ for } i = 1, \dots, s \end{cases} \quad (20)$$

where s denote number of activated nodal contact pairs, $\boldsymbol{\lambda}_N = [\lambda_N^1 \lambda_N^2 \dots \lambda_N^s]^T$ represents the normal contact force vector, λ_N^i represents the Lagrange multiplier for the i^{th} nodal contact pair, and $\mathbf{g}_N = [\mathbf{g}_N^1 \mathbf{g}_N^2 \dots \mathbf{g}_N^s]^T$. In the Lagrange multipliers, $\boldsymbol{\lambda}_N$ is treated as an unknown and Eq. (20) is solved simultaneously.

2.4.3 Numerical solution of motion equation in contact

The forward increment Lagrange multipliers method is used for the time-integration of Eqs. (20) and (11) [51]. The constrained equation of motion is expressed as follows:

$$\begin{cases} \mathbf{M}\ddot{\mathbf{d}}^n + \mathbf{C}\dot{\mathbf{d}}^n + \mathbf{K}\mathbf{d}^n + (\mathbf{G}_N^{n+1})^T \boldsymbol{\lambda}_N^n + \mathbf{K}_{\mathbf{u}\varphi}^{pu} \varphi^{pu,n} + \mathbf{K}_{\mathbf{u}\varphi}^{pr} \varphi^{pr,n} = 0 \\ \mathbf{G}_N^{n+1}(\mathbf{d}^{n+1} + \delta \mathbf{e}_S) = 0 \\ Q^{pu,n} = \int \int_{A^{pu}} (\mathbf{e}\mathbf{B}_u) dA d^n + C^{pu} \varphi^{pu,n} \\ Q^{pr,n} = \int \int_{A^{pr}} (\mathbf{e}\mathbf{B}_u) dA d^n + C^{pr} \varphi^{pr,n} \\ L^{pu} \ddot{Q}^{pu,n} + \varphi^{pu,n} = \varphi_{inp}^{pu,n} \\ L^{pr} \ddot{Q}^{pr,n} + \varphi^{pr,n} = \varphi_{inp}^{pr,n} \\ \mathbf{K}_{\varphi\varphi}^s \varphi^{s,n+1} = -\mathbf{K}_{\varphi\mathbf{u}}^s \mathbf{d}^{n+1} \end{cases} \quad (21)$$

At the current time t^n , it is assumed that no contact exists. The central difference time integration is used for solution of Eq. (21) for the next increment (t^{n+1}):

$$\begin{bmatrix} \mathbf{a}_{11} & \mathbf{0} & \mathbf{0} & \mathbf{a}_{14} \\ \mathbf{a}_{12} & a_{22} & 0 & 0 \\ \mathbf{a}_{31} & 0 & a_{33} & 0 \\ (\mathbf{a}_{14})^T & \mathbf{0} & \mathbf{0} & \mathbf{0} \end{bmatrix} \begin{bmatrix} \mathbf{d}^{n+1} \\ \varphi^{pu,n+1} \\ \varphi^{pr,n+1} \\ \boldsymbol{\lambda}_N^{n+1} \end{bmatrix} = \begin{bmatrix} \mathbf{b}_1 \\ b_2 \\ b_3 \\ \mathbf{b}_4 \end{bmatrix} \quad (22)$$

Appendix A provides details of Eq. (22). By solving Eq. (A.1), the displacement (\mathbf{d}^{n+1}), voltage of the probe ($\varphi^{pr,n+1}$) and pump ($\varphi^{pu,n+1}$) actuator, as well as the contact force (λ_N^n) in the next time step (t^{n+1}) are calculated.

The proposed method's performance is assessed using a DI, which is the average of the sideband's amplitude [1] as follow:

$$DI = \frac{\sum_{i=0}^n (A_{sb}^{i,+} + A_{sb}^{i,-})}{n} \quad (23)$$

where $A_{sb}^{i,+}$ and $A_{sb}^{i,-}$ are the i^{th} right and left sidebands, respectively and n is the number of sidebands.

The properties of the materials used to model the beam are listed in Table (1).

Table 1: aluminum and PZT properties

Parameter	PZT-5H	aluminum
c_{11} (Nm^{-2})	129×10^9	91.9×10^9
c_{13} (Nm^{-2})	84.1×10^9	45.3×10^9
c_{33} (Nm^{-2})	117.9×10^9	91.9×10^9
c_{44} (Nm^{-2})	23.9×10^9	23.9×10^9
e_{31} (Cm^{-2})	-6.5	0
e_{33} (Cm^{-2})	23	0
e_{15} (Cm^{-2})	17.44	0
ϵ_{11} (Fm^{-1})	15.03×10^{-9}	0
ϵ_{33} (Fm^{-1})	13×10^{-9}	0
ρ (kgm^{-3})	7500	2700

Figure (4) shows the results of applying the proposed method (circuit with an inductor) and comparing it to the conventional method (circuit without an inductor) at pump frequency 56 kHz and carrier frequency 250 kHz. Also, the magnified frequency response around the carrier frequency is shown in this figure. All higher harmonics are filtered out because this study is only interested in the intermodulation effect.

As shown in Figures (4a) and (4c), the sidebands do not appear in the frequency response of the sensor output without and with inductor in the healthy state, respectively. In the defective state, however, sidebands are visible in the sensor's frequency response. Also, the amplitude of the frequency response in conventional method is much less than the proposed method (Figures (4b) and (4d)). In addition, the number of sidebands in the proposed method is 4, while the number of sidebands in the conventional method is 2. Therefore, the use of inductors has increased both the amplitude and number of sidebands, which is an advantage of the proposed method over the previous method. For NWM without and with the inductor, the DIs are 2.1×10^{-5} and 35×10^{-5} , respectively. The DI when using the inductor is seventeen times higher than when it is not used.

3 Experiments

This section describes the circuits needed to implement the NWM with the inductor. The proposed method will next be tested for damage detection on two experimental setups, including an aluminum beam with loosened boundary and a sandwich panel with a loosened bolt, employing these circuits.

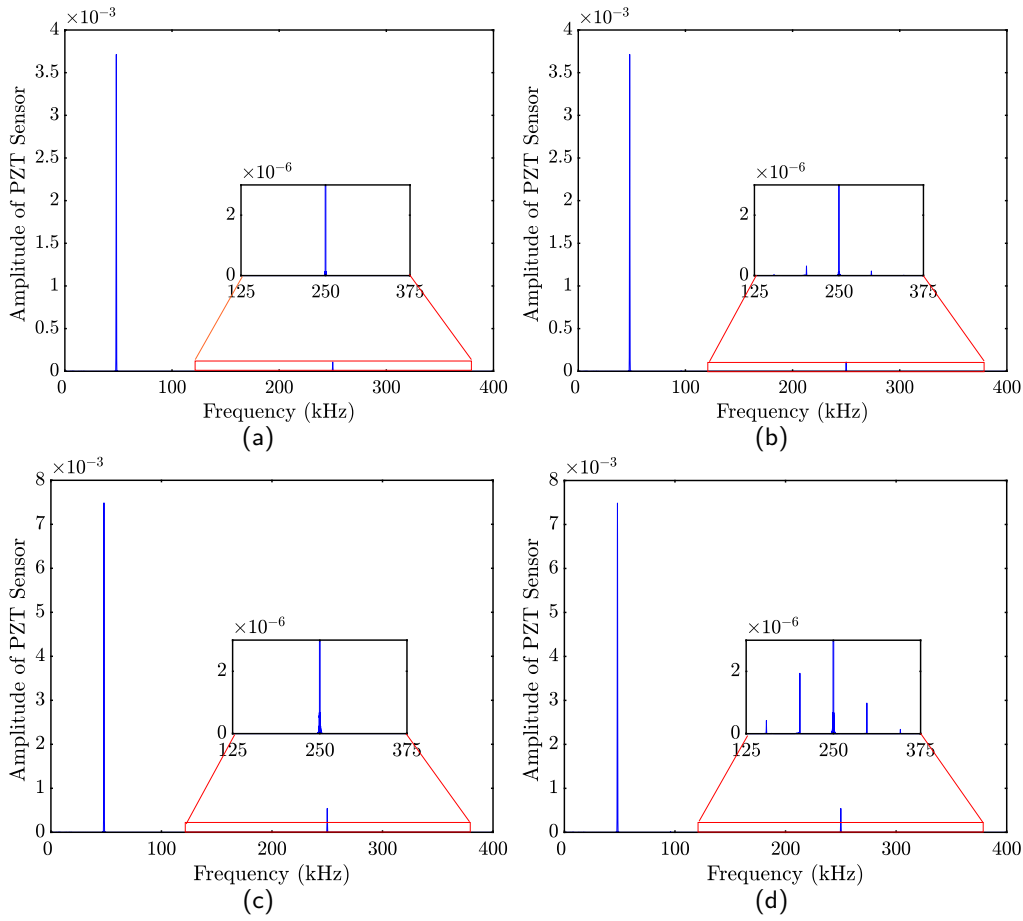


Fig. 4: Frequency response of the PZT sensor with focusing around carrier frequency at pump frequency 56 kHz and carrier frequency 250 kHz a) healthy structure without inductor b) defected structure without inductor c) healthy structure with inductor d) defected structure with inductor

3.1 Hardware design

Figure (5) shows a schematic of relays, waveform generator, inductors, and PZTs. A microcontroller has the duty of sending required settings for low and high-frequency harmonic signals to signal generators (AD9833) through a Serial Peripheral Interface (SPI). Moreover, it controls two sets of relays, making different inductances by short-circuiting specific inductors connected in series. The pump and carrier are driven by two sets of wave generators and inductors. AD9833 is a digitally controllable waveform generator capable of producing sine waves up to 12.5 MHz with 28-bit resolution so that a 0.004 Hz frequency step is achievable. AD9833 is powered by an evaluation board and connected to the microcontroller via the SPI interface. Since output voltage and current of AD9833 are not enough to drive PZT transducers and it has a DC offset, it is required to be amplified and remove the offset. It is done using an OP37 operational amplifier (op-amp) in a non-inverting mode with a capacitor on the input. The gain is set such that output swings between

$\pm 6.5\text{V}$. The indicator's value must be selected according to a specific resonance frequency of the PZT series to the inductor. Six different frequencies are selectable with three connected inductors to each transducer. The microcontroller decides which relays to power on based on the required inductance and capacitance of the transducer and shorts out unnecessary inductors. With just three inductors, a wide range of frequencies can be achieved. It is the same for both pump PZT and carrier PZT. The output amplitude of the sensor PZT is bipolar and usually between -5 to $+5$

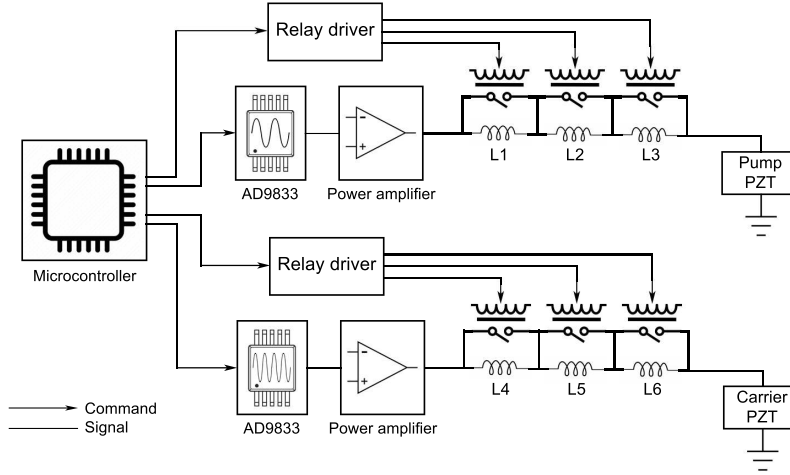


Fig. 5: Schematic of controller relays, waveform generator, inductors and PZTs

V, while the input of ADC accepts unipolar signals between 0 to 3.3 V. An op-amp can achieve a bias of 1.65 V directly after the sensor with gain and offset adjustments. High pass filters are placed within the same op-amp to mitigate low-frequency noise such as 50 Hz. To prevent aliasing, a low-pass filter is applied to the signal before it is fed into the converter. A 12-bit ADC is used for this part, which provides enough resolution for further signal processing. The piezoelectric transducers act as a capacitor in a simplified model. The impedance of a capacitive load decreases as frequency increases. Therefore, a large current or power is required to drive a capacitive load at higher frequencies leading to a much more complex and expensive amplifier. There are a few assumptions for designing this amplifier:

- Maximum output power is 70 Watts, approximately
- Bandwidth is around 0.5-700 kHz
- Maximum Total Harmonic Distortion (THD) should be below 1%

3.2 Design and fabrication of the power amplifier

Step 1: The maximum capacitance of the load should be considered. Given that to monitor the structure's health, the dimensions of the actuator have certain limits and the capacitance depends on the dimensions, a capacitance equal to 20 nF is considered.

Step 2: Defining the slew rate. The maximum frequency and voltage must be considered to determine the slew rate. The slew rate for a sine wave is calculated as follows:

$$\text{slew rate [V}/\mu\text{s}] = 2\pi f \cdot V_{\text{out}} \left(10^{-6}\right) \quad (24)$$

Step 3: The maximum output current required for the load depends on the maximum frequency and output voltage. Each amplifier usually has several stages. Each stage should have a large enough input impedance so that the previous stage does not affect the next stage, and at the same time, it should have a low output impedance to have minor effects on the next stages or to be able to deliver enough power to the load. In this design, two stages are considered. The first stage benefits an op-amp to have a large input impedance. Therefore, the output signal from the wave generator is not affected by the op-amp. The first stage is also used for voltage amplification. However, op-amps usually have high output impedance, hence, minor output current, so they do not perform well driving capacitive loads specifically, at higher frequencies. In the second stage, a class AB common-emitter push-pull amplifier was used to amplify the current and drive the load. This stage has a low output impedance, high current gain, proper frequency characteristic and low distortion (Figure (6)). Another issue to consider is the power dissipation of the op-amp and the push-pull stage which, is resolved by a proper heat sink for each stage. It depends on the transistor's junction temperature to determine how much power it can deliver. Therefore, when the transistor is adequately cooled, it can transfer more power and operate at maximum power. Table (2) shows the specifications of the proposed amplifier for a 20 nF capacitor as a load and a

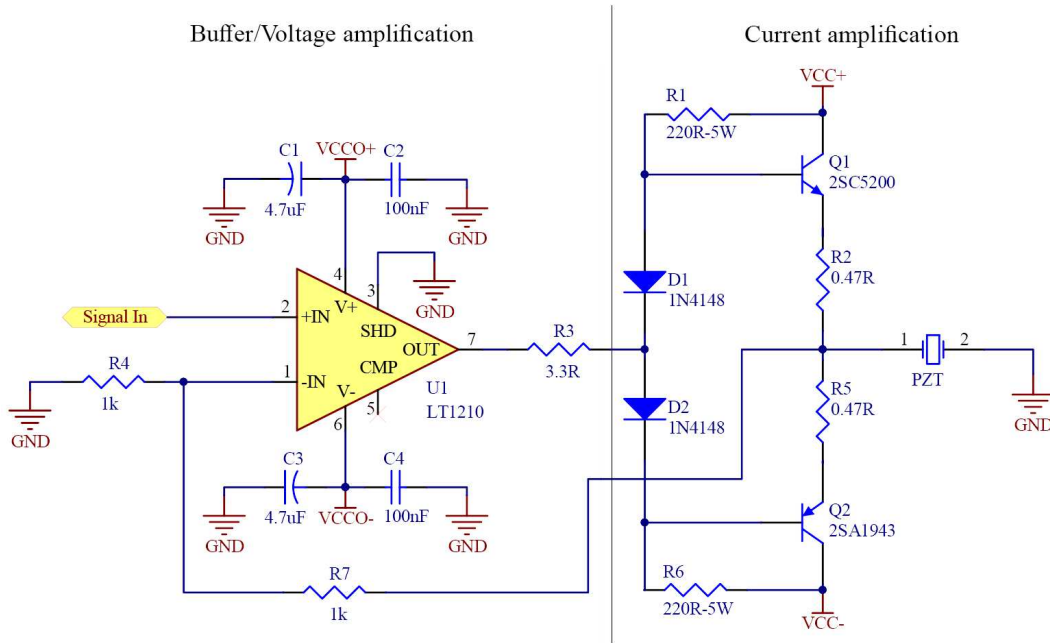


Fig. 6: Schematic of power amplifier circuit

maximum frequency of 800 kHz (maximum load condition). Experimentally measured frequency response for different capacitances is shown in Figure (7). With increasing capacitance of the load,

the cut-off frequency decreases. Thus, if the capacitance of the transducer is less than 10 nF, the amplifier can be used without reduction in output voltage up to 2 MHz. According to the phase diagram, the phase shift of the output signal relative to the input is always less than 10 degrees up to 1 MHz, which is acceptable for practical applications such as the one in this paper.

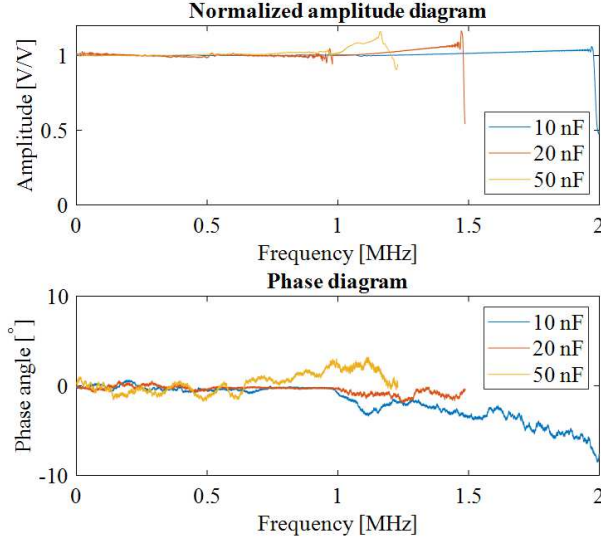


Fig. 7: Frequency response of proposed power amplifier for different loads

Table 2: Specifications for power amplifier at the maximum load (20 nF capacitance)

Parameter	Value
Peak to peak	25 V
Maximum current	3A
Slew rate	700V/ μ s
THD	0.8%

Table (3) provides values for inductors used in this study measured with a RLC meter. As it can be seen from this table, the inherent resistance of an inductor is a very small value that can almost be ignored in calculations.

To determine the exact experimental value of the resonant frequency of an inductor and PZT circuit, first the approximate frequency range in which the inductor and PZT resonate is calculated theoretically. Then, a chirp signal is applied to the entire pump/probe circuit, including the actuator and the inductor. After the chirp signal is applied, the sensor's output frequency is measured. Thus, the resonant frequency is defined as the frequency at which the sensor's frequency response reaches its maximum amplitude. Those frequencies are shown in Table (4) for each actuator and inductor.

Table 3: The inductance and inherent resistance of inductor measured by RLC meter

Symbol	Inductance (μH)	Resistance ($\text{m}\Omega$)
L1	50.01	250.5
L2	100.02	300.3
L3	120.01	330.2
L4	350.04	600.5
L5	500.03	780.1
L6	998.6	950.5

Table 4: Different combination of pump and carrier inductors in series with transducers ($\approx 8.1 \text{ nF}$) to get different resonance frequencies

Pump Inductance	Frequency (kHz)	Carrier Inductance	Frequency (kHz)
L1	250	L4	94.8
L2	176.9	L5	79.3
L3	161.5	L6	56
L1+L2	144.4	L4+L5	61
L1+L3	135.3	L4+L6	48.5
L2+L3	119.2	L5+L6	46

4 Enhanced NWM with coupled-inductor

4.1 Aluminum Beam

The results of the NWM with the inductor for the aluminum beams are reported in this section. The loosening of the boundary is considered as damage in this section (Figure (8)). Figure (1) shows the pump, carrier actuator, and piezoelectric sensors. To compare the NWM with and without

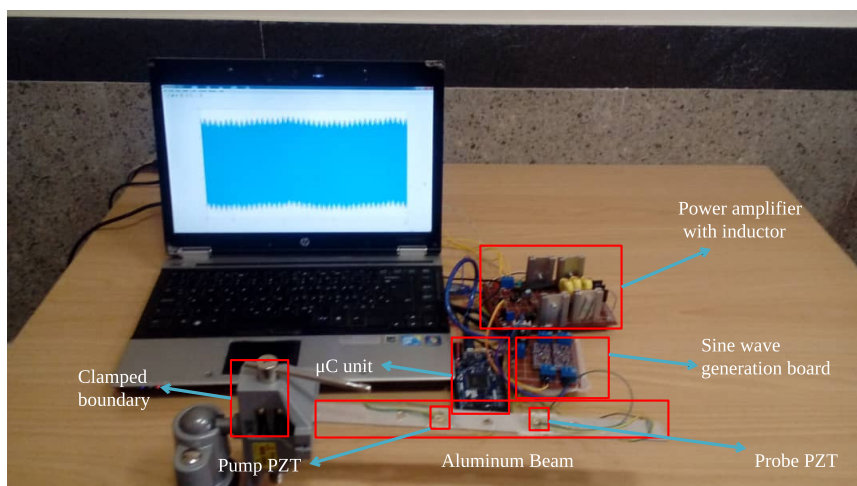


Fig. 8: The experimental setup of cantilever aluminum beam with loosening of the boundary condition as defect

an inductor, the results are first measured for the state with a tight boundary (healthy state), and then the results are obtained for the state with a loose boundary (defected state). Figure (9) illustrates the healthy and defected state results for the NWM with and without the inductor for the 61 kHz pump frequency and the 250 kHz carrier. In this case, the pump inductor (L1) and the carrier inductor (L4) are chosen according to Figure (5) and Table (4). Since the structure is in healthy state, no significant nonlinearity is present and only the excitation frequencies are visible in the sensor frequency response, as seen in Figures (9a) and (9b).

The resonance amplitude in a tank circuit depends on the amount of capacitors and inductors. As a result, the pump amplitude ratio in Figures (9c) and (9a) (about seven times) is different from the probe amplitude ratio in the same figures (about five times). This is due to the different amounts of the inductors in the pump and probe circuits (Table (4)).

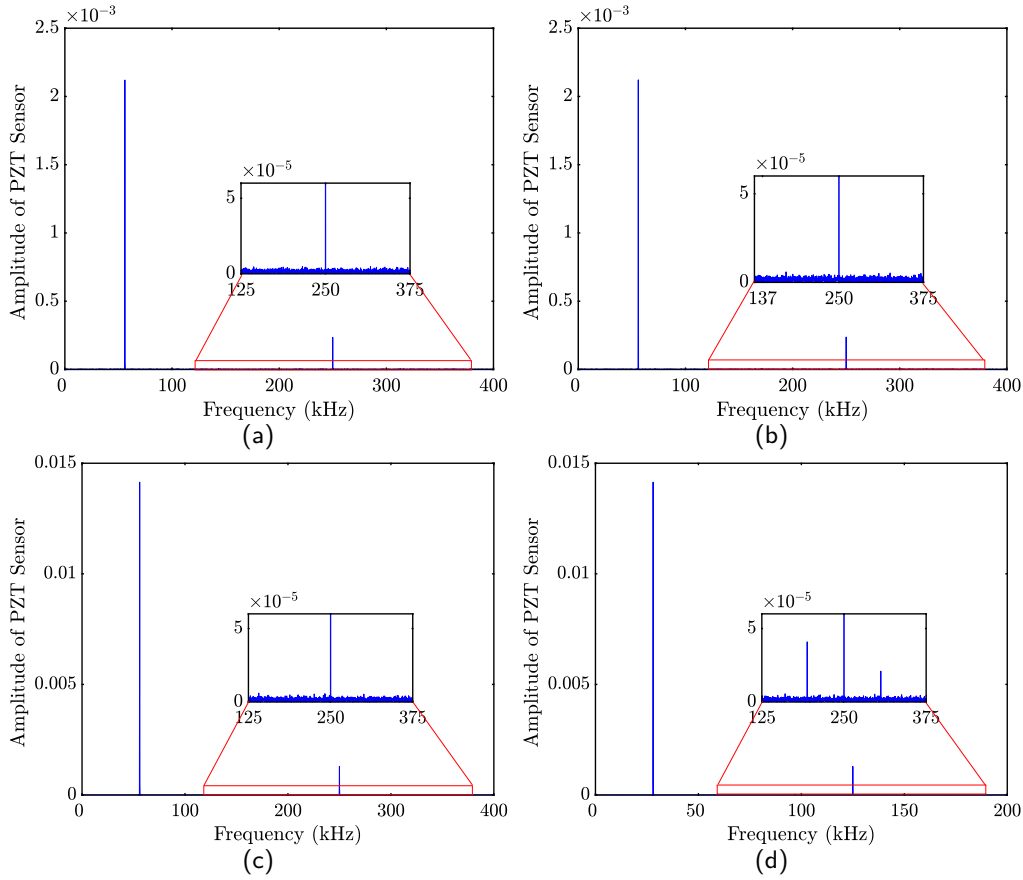


Fig. 9: Frequency response of the PZT sensor magnified on carrier frequency at pump frequency 61 kHz and carrier frequency 250 kHz a) healthy structure without inductor b) defected structure without inductor c) healthy structure with inductor d) defected structure with inductor

For defected state, sidebands are not present in the results of the NWM without the inductor, as shown in Figure (9b), but they exist when the inductor was used (Figure (9d)). Figure (10) shows

the result of the NWM with and without inductor for the healthy and defected states at pump and carrier frequencies of 56 kHz and 250 kHz, respectively. The results of both the conventional method and the proposed method for SFEM (Figure (4)) and experimental results (Figure (10)) are in good agreement.

Figures (9c) and (10c) show the results of the healthy state and the designed circuit (Figure (6)) with the inductor. There is no sideband in the results of the healthy state of the structure in this case. Therefore, the circuit alone does not produce sidebands, and the sidebands shown in Figures (9d) and (10d) are only due to the loosening of the boundary. The same results were obtained for all frequency combinations related to Table (4), showing that, in the healthy state, no sideband is generated from any combination of probe and pump frequencies. At all of these frequencies, the circuit does not cause a nonlinear factor. The nonlinear characteristics created by the boundary looseness tests are only due to the boundary looseness itself. It can be seen that only excitation frequencies (pump and carrier) are visible, as shown in Figure (10) for the healthy state. The sidebands are also visible in the frequency response of the defected case in the NWM without the inductor. However, the proposed method has more sidebands with a larger amplitude than the NWM without the inductor.

Finally, Table (5) shows the DIs for the carrier and pump actuator using a combination of inductors using the NWM with and without the inductor. This table only shows the DI for a limited number of pump and carrier frequencies. This table shows that the NWM with the inductor has a

Table 5: Comparison of DIs between the NWM without inductor for aluminum beam

Pump frequency	Carrier frequency	DI without inductor	DI with inductor	sideband # without inductor	sideband # with inductor
46kHz	176.9kHz	3.5×10^{-3}	30×10^{-3}	2	5
48.5kHz	161.5kHz	2.3×10^{-3}	18×10^{-3}	2	4
56kHz	176.9kHz	-	13×10^{-3}	-	2
61kHz	135.3kHz	2.7×10^{-3}	25×10^{-3}	2	4
79.3kHz	144.4kHz	-	8×10^{-3}	-	3
94.8kHz	250kHz	1.5×10^{-3}	16×10^{-3}	2	2

higher DI than the NWM without the inductor. Furthermore, in some cases of the NWM without the inductor, the DI is not detectable, meaning that the damage is not detected. In contrast, in the same cases of the proposed method, the DI is non-zero, indicating that the damage has been discovered. A 10 V voltage is applied to the pump and carrier without an inductor. Piezoelectric pumps have maximum and minimum voltages that depend on frequency, e.g., 50 V and 70 V if the inductor is used. The probe piezoelectric has a maximum and minimum voltage of 60 V and 90 V, respectively.

4.2 Sandwich panel

4.2.1 Investigation of bolt looseness

This section will look at the sandwich panel results. The sandwich panel has a dimension of $200 \times 20 \times 12$ mm. The skin thickness is 1 mm, and the core thickness is 10 mm. The skin is made of aluminum, and the core material is polyethylene. The experimental setup and schematic for the sandwich beam with three piezoelectric patches are shown in Figure (11). The loosening of the

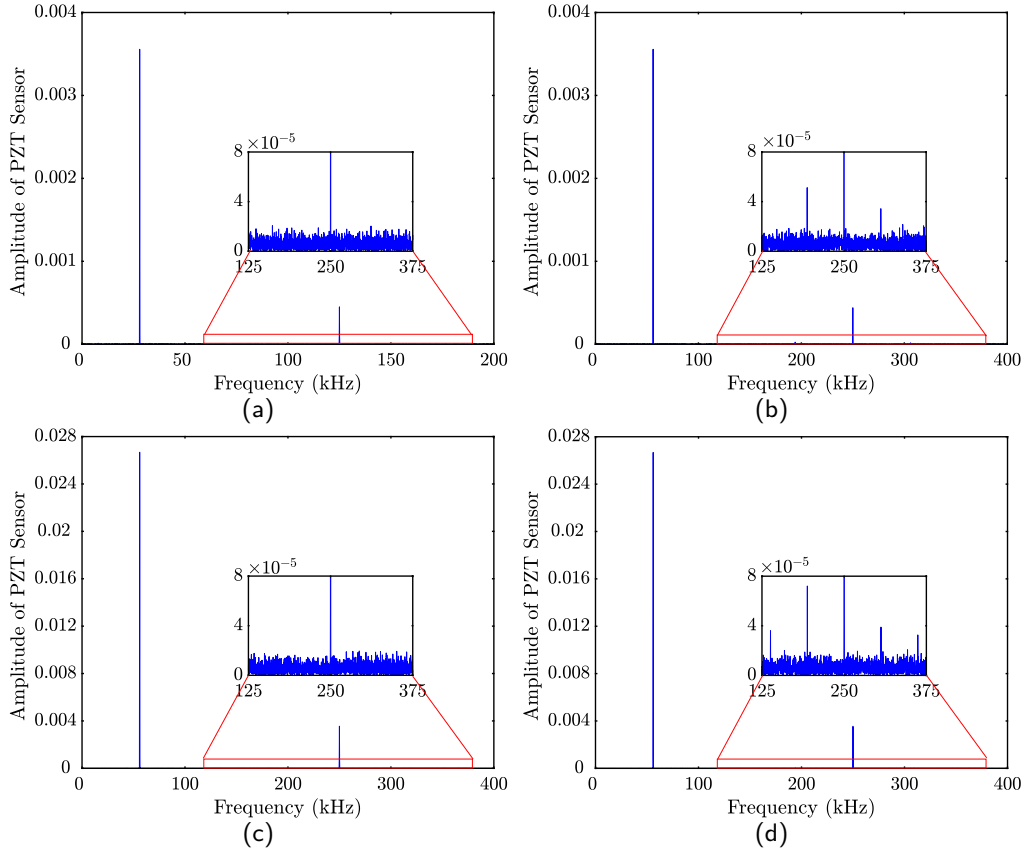


Fig. 10: Frequency response of the PZT sensor with focusing around carrier frequency at pump frequency 56 kHz and carrier frequency 250 kHz a) healthy structure without inductor b) defected structure without inductor c) healthy structure with inductor d) defected structure with inductor

bolt is interpreted as damage in the beam. In this section, the same inductors as defined in Table (4) are used.

Table (6) shows the DI for the NWM with and without the inductor. This table contains DIs for a few combinations of pump and carrier frequencies, not all of them. The DI has led to better damage detection in the NWM with the inductor, as shown in this table. According to this table, when the inductor was used a higher DI than when the inductor was not used, similar to the aluminum beam. Furthermore, in some cases of the NWM without the inductor, the DI is not detectable, indicating that the defect is not detected. In contrast, in the same cases of the proposed method, the DI is non-zero. This means that the proposed method was able to detect the damage. Also, the NWM without the inductor has a maximum of two recognizable sidebands, whereas the NWM with the inductor has a maximum of five recognizable sidebands.

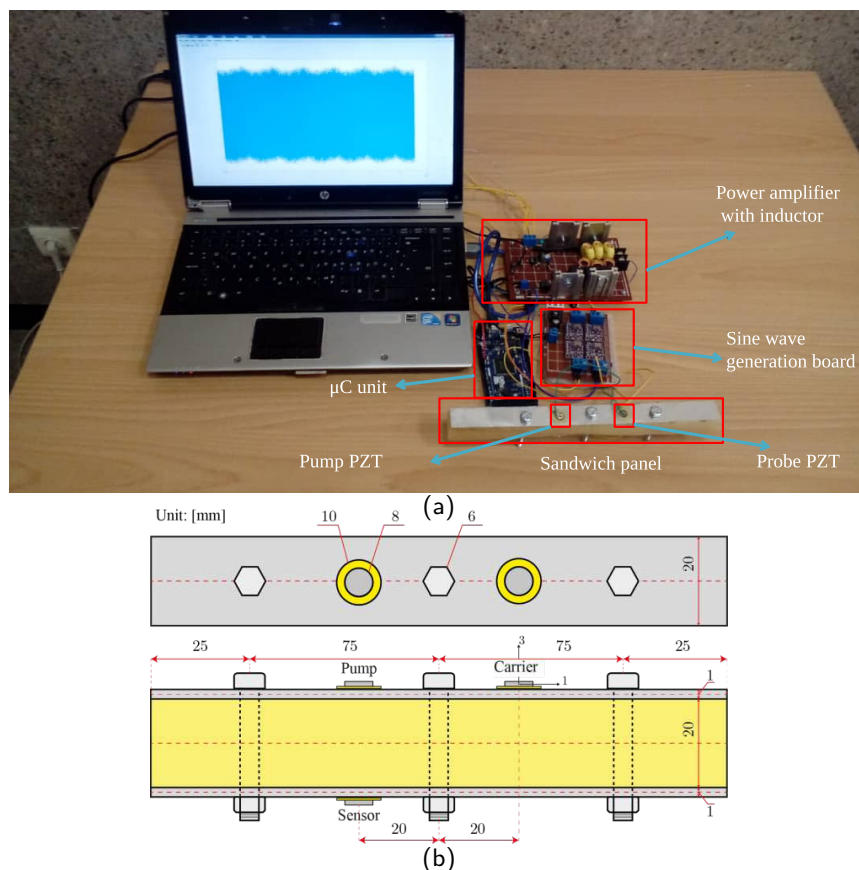


Fig. 11: The experimental setup for free the sandwich panel with loosening of the bolt as defect
(b) schematic of the sandwich panel

Table 6: Comparison of the DI between the NWM with and without inductor for sandwich panel

Pump frequency	Carrier frequency	DI without inductor	DI with inductor	sideband # without inductor	sideband # with inductor
46kHz	176.9kHz	2×10^{-3}	17×10^{-3}	2	4
48.5kHz	161.5kHz	-	8×10^{-3}	-	3
56kHz	176.9kHz	5×10^{-3}	27×10^{-3}	2	5
61kHz	135.3kHz	-	11×10^{-3}	-	3
79.3kHz	144.4kHz	3×10^{-3}	19×10^{-3}	2	4
94.8kHz	250kHz	1×10^{-3}	15×10^{-3}	2	2

4.2.2 Investigation of defect severity

This section examines the loosening severity of bolts for a probe frequency of 46kHz and a pump frequency of 176.9kHz. It is studied in both cases without and with inductors for three different severity of the damage. To measure the torque of the bolt, a torque meter is used. Table (7) shows

the results of the DI for different damage based on severity. Increasing bolt loosening increases DI

Table 7: Comparison of the DI between the NWM with and without inductor for different severity of damage

Damage #	Torque (N.m)	DI with inductor	DI without inductor
1	10	–	4×10^{-3}
2	5	1.1×10^{-3}	10×10^{-3}
3	1	2×10^{-3}	17×10^{-3}

both with and without inductors, as shown in this table. In damage # 1, however, it was impossible to diagnose the damage without the inductor. Additionally, DIs for all severity levels of damage are significantly higher in the presence of inducer compared to the absence of inducer. Moreover, when the inductor is used, it can even detect damage # 1.

5 Conclusion

This article presents a low-cost and portable method for improving the performance of NWM. At the resonant frequency of the series inductor and actuator PZT, the applied voltage on the actuator PZT is greater than that of the NWM without the inductor, which is about ten volts. First, a spectral finite element model was used to assess the feasibility of the proposed method. According to the results, the DI increases when an inductor is included in the model. A low-cost power amplifier was designed and built to provide the resonant circuit current in the experimental part. The proposed method was tested on two experimental setups: an aluminum beam with a loose boundary and a sandwich panel with a loosened bolt as damage. For all frequency combinations, aluminum and sandwich structures, the healthy state results showed no sidebands caused by the inductor design, so all sidebands related to the defect are merely a result of the damage. Both with and without inductors, the models and experimental results for boundary loosening in aluminum beams were in good agreement. Both experimental setups demonstrated that the proposed method increases the DI. The DI has increased more than seven times for the aluminum beam and at least five times for the sandwich panel compared to the NWM without the inductor. There are also frequencies in both experimental setups where the DI is not detectable, indicating that the NWM could not detect the damage without the inductor. Conversely, the DI in the NWM with the inductor is nonzero in the same frequencies, indicating that the NWM with the inductor has identified the defect. Also, the results of damage severity were examined, and it was found that all of the results in which the inductor was used had a much larger DI compared to the results in which it was not used.

A Appendix A

The matrix and vector entries of Eq. (22) are defined as follow:

$$\begin{aligned} \mathbf{a}_{11} &= \frac{\mathbf{M}}{h^2} + \frac{\mathbf{C}}{h} \\ \mathbf{a}_{14} &= \left(\mathbf{G}_N^{n+1} \right)^T \\ \mathbf{a}_{12} &= \frac{L^{pu}}{\Delta T^2} \iint_{A^{pu}} (\mathbf{eB}_u) dA \end{aligned}$$

$$\begin{aligned}
a_{22} &= \frac{L^{pu}}{\Delta T^2} C^{pu} \\
a_{31} &= \frac{L^{pr}}{\Delta T^2} \int \int_{A^{pr}} (\mathbf{eB}_u) dA \\
a_{33} &= \frac{L^{pr}}{\Delta T^2} C^{pr} \\
b_1 &= -\mathbf{K}_{u\varphi}^{pu} \varphi^{pu,n} - \mathbf{K}_{u\varphi}^{pr} \varphi^{pr,n} - \mathbf{K} \mathbf{d}^n + \left(-\frac{\mathbf{M}}{\Delta T^2} + \frac{\mathbf{C}}{\Delta T} \right) \mathbf{d}^{n-1} + 2 \frac{\mathbf{M}}{\Delta T^2} \mathbf{d}^n \\
b_2 &= -\varphi^{pu,n} + \varphi_{inp}^{pu,n} + L^{pu} \left(\frac{\int \int_{A^{pu}} (\mathbf{eB}_u) dA (-\mathbf{d}^{n-1} + 2\mathbf{d}^n)}{\Delta T^2} \right. \\
&\quad \left. + \frac{C^{pu} (-\varphi^{pu,n-1} + 2\varphi^{pu,n})}{\Delta T^2} \right) \\
b_3 &= -\varphi^{pr,n} + \varphi_{inp}^{pr,n} + L^{pr} \left(\frac{\int \int_{A^{pr}} (\mathbf{eB}_u) dA (-\mathbf{d}^{n-1} + 2\mathbf{d}^n)}{\Delta T^2} \right. \\
&\quad \left. + \frac{C^{pr} (-\varphi^{pr,n-1} + 2\varphi^{pr,n})}{\Delta T^2} \right) \\
b_4 &= -\mathbf{G}_N^{n+1} \delta \mathbf{e} \mathbf{s}
\end{aligned} \tag{A.1}$$

Conflict of Interest

The authors declare that they have no conflict of interest.

Funding

The author(s) received no financial support for the research, authorship, and/or publication of this article.

Data availability

The datasets generated during and/or analysed during the current study are available from the corresponding author on reasonable request.

References

1. Donskoy, D., Liu, D.: Vibro-acoustic modulation baseline-free non-destructive testing. *Journal of Sound and Vibration* 492, 115808 (2021)
2. Donskoy, D.M., Ramezani, M.: Separation of amplitude and frequency modulations in vibro-acoustic modulation nondestructive testing method. In: *Proceedings of Meetings on Acoustics 21ISNA*. vol. 34, p. 045002. Acoustical Society of America
3. Sepehry, N., Ehsani, M., Zhu, W., Bakhtiari-Nejad, F.: Application of scaled boundary finite element method for vibration-based structural health monitoring of breathing cracks. *Journal of Vibration and Control* p. 1077546320968646 (2020)
4. Van Den Abeele, K.A., Carmeliet, J., Ten Cate, J.A., Johnson, P.A.: Nonlinear elastic wave spectroscopy (news) techniques to discern material damage, part ii: Single-mode nonlinear resonance acoustic spectroscopy. *Journal of Research in Nondestructive Evaluation* 12(1), 31–42 (2000)
5. Van Den Abeele, K.A., Johnson, P.A., Sutin, A.: Nonlinear elastic wave spectroscopy (news) techniques to discern material damage, part i: nonlinear wave modulation spectroscopy (nwms). *Journal of Research in Nondestructive Evaluation* 12(1), 17–30 (2000)

6. Sepehry, N., Asadi, S., Shamshirsaz, M., Bakhtiari Nejad, F.: A new model order reduction method based on global kernel k-means clustering: Application in health monitoring of plate using Lamb wave propagation and impedance method. *Structural Control and Health Monitoring* 25(9), e2211 (2018)
7. Sepehry, N., Shamshirsaz, M., Bakhtiari Nejad, F.: Low-cost simulation using model order reduction in structural health monitoring: Application of balanced proper orthogonal decomposition. *Structural Control and Health Monitoring* 24(11), e1994 (2017)
8. Sepehry, N., Shamshirsaz, M., Bastani, A.: Experimental and theoretical analysis in impedance-based structural health monitoring with varying temperature. *Structural Health Monitoring* 10(6), 573–585 (2011)
9. Jang, J., Liu, P., Kim, B., Kim, S.w., Sohn, H.: Silicon wafer crack detection using nonlinear ultrasonic modulation induced by high repetition rate pulse laser. *Optics and Lasers in Engineering* 129, 106074 (2020)
10. Kim, S., Adams, D.E., Sohn, H., Rodriguez-Rivera, G., Myrent, N., Bond, R., Vitek, J., Carr, S., Grama, A., Meyer, J.J.: Crack detection technique for operating wind turbine blades using vibro-acoustic modulation. *Structural Health Monitoring* 13(6), 660–670 (2014)
11. Sepehry, N., Bakhtiari-Nejad, F., Shamshirsaz, M.: Discrete singular convolution and spectral finite element method for predicting electromechanical impedance applied on rectangular plates. *Journal of Intelligent Material Systems and Structures* 28(18), 2473–2488 (2017)
12. Sepehry, N., Bakhtiari-Nejad, F., Shamshirsaz, M., Zhu, W.: Nonlinear modeling of cracked beams for impedance based structural health monitoring. In: *ASME International Mechanical Engineering Congress and Exposition*. vol. 58387, p. V04BT05A034. American Society of Mechanical Engineers
13. Pieczonka, L., Klepka, A., Martowicz, A., Staszewski, W.J.: Nonlinear vibroacoustic wave modulations for structural damage detection: an overview. *Optical Engineering* 55(1), 011005 (2015)
14. Zhang, M., Shen, Y., Xiao, L., Qu, W.: Application of subharmonic resonance for the detection of bolted joint looseness. *Nonlinear Dynamics* 88(3), 1643–1653 (2017)
15. Li, Q., Jing, X.: A second-order output spectrum approach for fault detection of bolt loosening in a satellite-like structure with a sensor chain. *Nonlinear Dynamics* 89(1), 587–606 (2017)
16. Jing, X., Li, Q.: A nonlinear decomposition and regulation method for nonlinearity characterization. *Nonlinear Dynamics* 83(3), 1355–1377 (2016)
17. Yang, Y., Ng, C.T., Kotousov, A.: Bolted joint integrity monitoring with second harmonic generated by guided waves. *Structural Health Monitoring* 18(1), 193–204 (2019)
18. Ingard, U., Pridmore-Brown, D.C.: Scattering of sound by sound. *The Journal of the Acoustical Society of America* 28(3), 367–369 (1956)
19. Solodov, I.Y., Krohn, N., Busse, G.: Can: an example of nonclassical acoustic nonlinearity in solids. *Ultrasonics* 40(1-8), 621–625 (2002)
20. Westervelt, P.J.: Scattering of sound by sound. *The Journal of the Acoustical Society of America* 29(2), 199–203 (1957)
21. Donskoy, D.M., Sutin, A.M.: Vibro-acoustic modulation nondestructive evaluation technique. *Journal of intelligent material systems and structures* 9(9), 765–771 (1998)
22. Wang, F., Song, G.: Bolt early looseness monitoring using modified vibro-acoustic modulation by time-reversal. *Mechanical Systems and Signal Processing* 130, 349–360 (2019)
23. Meyer, J.J., Adams, D.E.: Theoretical and experimental evidence for using impact modulation to assess bolted joints. *Nonlinear Dynamics* 81(1), 103–117 (2015)
24. Wang, F., Song, G.: Monitoring of multi-bolt connection looseness using a novel vibro-acoustic method. *Nonlinear Dynamics* 100(1), 243–254 (2020)
25. Amerini, F., Meo, M.: Structural health monitoring of bolted joints using linear and nonlinear acoustic/ultrasound methods. *Structural health monitoring* 10(6), 659–672 (2011)
26. He, Y., Xiao, Y., Su, Z., Pan, Y., Zhang, Z.: Contact acoustic nonlinearity effect on the vibro-acoustic modulation of delaminated composite structures. *Mechanical Systems and Signal Processing* 163, 108161 (2022)
27. Yoder, N.C., Adams, D.E.: Vibro-acoustic modulation utilizing a swept probing signal for robust crack detection. *Structural Health Monitoring* 9(3), 257–267 (2010)
28. Zhang, Z., Liu, M., Liao, Y., Su, Z., Xiao, Y.: Contact acoustic nonlinearity (can)-based continuous monitoring of bolt loosening: Hybrid use of high-order harmonics and spectral sidebands. *Mechanical Systems and Signal Processing* 103, 280–294 (2018)
29. Zhang, Z., Liu, M., Su, Z., Xiao, Y.: Quantitative evaluation of residual torque of a loose bolt based on wave energy dissipation and vibro-acoustic modulation: A comparative study. *Journal of Sound and Vibration* 383, 156–170 (2016)
30. Zhang, Z., Xiao, Y., Xie, Y., Su, Z.: Effects of contact between rough surfaces on the dynamic responses of bolted composite joints: Multiscale modeling and numerical simulation. *Composite Structures* 211, 13–23 (2019)
31. Zhang, Z., Xu, H., Liao, Y., Su, Z., Xiao, Y.: Vibro-acoustic modulation (vam)-inspired structural integrity monitoring and its applications to bolted composite joints. *Composite Structures* 176, 505–515 (2017)

32. Li, N., Wang, F., Song, G.: New entropy-based vibro-acoustic modulation method for metal fatigue crack detection: An exploratory study. *Measurement* 150, 107075 (2020)
33. Joglekar, D.: Analysis of nonlinear frequency mixing in timoshenko beams with a breathing crack using wavelet spectral finite element method. *Journal of Sound and Vibration* 488, 115532 (2020)
34. Klepka, A., Staszewski, W.J., Jenal, R., Szvedo, M., Iwaniec, J., Uhl, T.: Nonlinear acoustics for fatigue crack detection—experimental investigations of vibro-acoustic wave modulations. *Structural Health Monitoring* 11(2), 197–211 (2012)
35. Prawin, J., Rama Mohan Rao, A.: Vibration-based breathing crack identification using non-linear intermodulation components under noisy environment. *Structural Health Monitoring* 19(1), 86–104 (2020)
36. Zagrai, A., Donskoy, D., Chudnovsky, A., Golovin, E.: Micro-and macroscale damage detection using the nonlinear acoustic vibro-modulation technique. *Research in Nondestructive Evaluation* 19(2), 104–128 (2008)
37. Aymerich, F., Staszewski, W.J.: Impact damage detection in composite laminates using nonlinear acoustics. *Composites Part A: Applied Science and Manufacturing* 41(9), 1084–1092 (2010)
38. Chen, B.Y., Soh, S.K., Lee, H.P., Tay, T.E., Tan, V.B.: A vibro-acoustic modulation method for the detection of delamination and kissing bond in composites. *Journal of Composite Materials* 50(22), 3089–3104 (2016)
39. Pieczonka, L., Ukowski, P., Klepka, A., Staszewski, W., Uhl, T., Aymerich, F.: Impact damage detection in light composite sandwich panels using piezo-based nonlinear vibro-acoustic modulations. *Smart Materials and Structures* 23(10), 105021 (2014)
40. Sohn, H., Lim, H.J., DeSimio, M.P., Brown, K., Derriso, M.: Nonlinear ultrasonic wave modulation for online fatigue crack detection. *Journal of Sound and Vibration* 333(5), 1473–1484 (2014)
41. Chrysochoidis, N.A., Barouni, A.K., Saravanos, D.A.: Delamination detection in composites using wave modulation spectroscopy with a novel active nonlinear acousto-ultrasonic piezoelectric sensor. *Journal of Intelligent Material Systems and Structures* 22(18), 2193–2206 (2011)
42. Lim, H.J., Song, B., Park, B., Sohn, H.: Noncontact fatigue crack visualization using nonlinear ultrasonic modulation. *Ndt & E International* 73, 8–14 (2015)
43. Liu, P., Sohn, H., Jeon, I.: Nonlinear spectral correlation for fatigue crack detection under noisy environments. *Journal of Sound and Vibration* 400, 305–316 (2017)
44. Ballard, E., Vezirov, S.Y., Pfeleiderer, K., Solodov, I.Y., Busse, G.: Nonlinear modulation technique for nde with air-coupled ultrasound. *Ultrasonics* 42(1-9), 1031–1036 (2004)
45. Ooijevaar, T., Rogge, M.D., Loendersloot, R., Warnet, L., Akkerman, R., Tinga, T.: Vibro-acoustic modulation-based damage identification in a composite skin-stiffener structure. *Structural health monitoring* 15(4), 458–472 (2016)
46. Liu, P., Lim, H.J., Yang, S., Sohn, H., Lee, C.H., Yi, Y., Kim, D., Jung, J., Bae, I.h.: Development of a “stick-and-detect” wireless sensor node for fatigue crack detection. *Structural Health Monitoring* 16(2), 153–163 (2017)
47. Oppermann, P., Dorendorf, L., Rutner, M., Renner, C.: Nonlinear modulation with low-power sensor networks using undersampling. *Structural health monitoring* p. 1475921720982885 (2020)
48. Singh, A.K., Chen, B., Tan, V.B., Tay, T.E., Lee, H.P.: A theoretical and numerical study on the mechanics of vibro-acoustic modulation. *The Journal of the Acoustical Society of America* 141(4), 2821–2831 (2017)
49. Sepehry, N., Ehsani, M., Asadi, S., Shamshirsaz, M., Nejad, F.B.: Fourier spectral element for simulation of vibro-acoustic modulation caused by contact nonlinearity in the beam. *Thin-Walled Structures* 174, 109112 (2022)
50. Klepka, A., Dziedzic, K., Mrówka, J., Górski, J.: Experimental investigation of modulation effects for contact-type interfaces in vibro-acoustic modulation tests. *Structural Health Monitoring* (2019)
51. Carpenter, N.J., Taylor, R.L., Katona, M.G.: Lagrange constraints for transient finite element surface contact. *International journal for numerical methods in engineering* 32(1), 103–128 (1991)